Observation of Magnetic Reconnection in a Region of Strong Turbulence

R. E. Ergun[1,2] , N. Pathak[2], M. E. Usanova[2], Y. Qi[2], T. Vo[2], J. L. Burch[3] , S. J. Schwartz[2], R. B. Torbert[3,4] , N. Ahmadi[2],
F. D. Wilder[5], A. Chasipis[2] , D. L. Newman[6], J. E. Stawarz[7], M. Hesse[8], D. L. Turner[9] , and D. Gershman[10]

[1] Department of Astrophysical and Planetary Sciences, University of Colorado, Boulder, CO 80303, USA; ree@lasp.colorado.edu
[2] Laboratory of Atmospheric and Space Sciences, University of Colorado, Boulder, CO 80303, USA
[3] Southwest Research Institute, San Antonio, TX 78238, USA
[4] University of New Hampshire, Durham, NH 03824, USA
[5] Department of Physics, University of Texas at Arlington, Arlington, TX 76019, USA
[6] Department of Physics, University of Colorado, Boulder, CO 80303, USA
[7] The Blackett Laboratory, Imperial College London, London SW7 2AZ, UK
[8] NASA Ames Research Center, Moffett Field, CA 94035, USA
[9] Johns Hopkins University Applied Physics Laboratory, Laurel, MD 20723, USA
[10] NASA, Goddard Space Flight Center, Greenbelt, MD 20771, USA

Abstract

We examine a rare and interesting observation of magnetic reconnection embedded in a large-scale region of strong turbulence in which magnetic field annihilation is energizing ions and electrons. The magnetic reconnection event is in Earth's magnetotail and is associated with enhanced energetic particle fluxes indicating local particle acceleration. Despite substantial electric and magnetic field fluctuations throughout the surrounding, large-scale region, the ongoing magnetic reconnection has many similar properties to laminar, 2D magnetic reconnection including Hall electric fields, Hall magnetic fields, a thin electron current sheet, and ion and electron jets. Notably, the electron jet emerging from the electron diffusion region (EDR) appears to transport sufficient off-diagonal momentum to infer that off-diagonal electron stress can support the reconnection electric field in the EDR even in a turbulent environment. Although the electron jet appears to be briefly (∼1 s) deflected or possibly interrupted by an electromagnetic disturbance, the reconnection appears to otherwise continue for a long period (∼30 minutes) as evidenced by a persistent ion jet. This particular finding implies that the fundamental electron-scale processes inside of the EDR in turbulent magnetic reconnection are not necessarily distinct from those in laminar magnetic reconnection. These observations provide direct confirmation that magnetic reconnection can not only be responsible for but also can continue in regions of large-scale turbulence. Because the electric and magnetic fields of strong turbulence are linked to particle acceleration, it follows that particle acceleration also can continue as a consequence of turbulent magnetic reconnection.

1. Introduction

Magnetic reconnection and turbulence are intricately coupled in a variety of plasmas. They appear to coexist in the solar wind (Gosling et al. 2005; Gosling 2007), Earth's subsolar region (Retinó et al. 2007; Burch et al. 2016), Earth's magnetotail (Eastwood et al. 2009; Ergun et al. 2018; Cozzani et al. 2021), laboratory plasmas (Ji et al. 2004), and in numerical simulations (Daughton 2003; Pritchett et al. 2012; Roytershteyn et al. 2013; Price et al. 2016, 2017). The association is complex; magnetic reconnection can generate turbulence (Price et al. 2016, 2017) and, in kind, turbulence can lead to small-scale, transitory "secondary" (Lapenta et al. 2006; Ergun et al. 2016b) or "electron-only" (Phan et al. 2018; Stawarz et al. 2019) magnetic reconnection as part of the turbulent dissipation process.

In Earth's magnetotail, magnetic reconnection (Øieroset et al. 2001; Torbert et al. 2018) enables magnetic field (B) annihilation over a large region and, at the same time, produces ion jets that transport plasma away from this region. Inflow from the low-β magnetotail lobes continues to transport electromagnetic energy into the surrounding region but does not necessarily replenish lost plasma. With fewer particles to absorb the electromagnetic energy, turbulence can erupt, resulting in strong ion and electron acceleration (Eastwood et al. 2009; Ergun et al. 2020a, 2020b). Despite the turbulence, magnetic reconnection appears to continue as evidenced by persistent ion jets and continuing electromagnetic energy conversion based on positive $J \cdot E$ (J is current density and E is electric field). However, the fundamental electron-scale physics of turbulent magnetic reconnection is not fully explored.

In this Letter, we report an observation near the electron diffusion region (EDR) of magnetic reconnection in a turbulent region of Earth's magnetotail. The observations are from the Magnetospheric Multiscale (MMS) mission (Burch et al. 2015), which has four satellites in a tetrahedral configuration. This particular event is analyzed in two other concurrent studies (Tang et al. 2022; Wang et al. 2022). Tang et al. (2022) investigate what appears to be fine structure in the electron distributions attributing it to a small guide field and meandering electrons, for which we offer an alternate interpretation. Tang et al. (2022) also assert local wave activity does not appreciably support the magnetic reconnection electric field, with which we concur. Wang et al. (2022) discuss the role of lower hybrid wave activity.

We show that this magnetic reconnection event has many of the same characteristics of collisionless, 2D, antiparallel, laminar reconnection (Drake et al. 2008; Eastwood et al. 2010; Hesse et al. 2014, 2018; Genestreti et al. 2018; Nakamura et al. 2018, 2019; Torbert et al. 2018). An ion jet and its reversal are evident. $\boldsymbol{J} \cdot \boldsymbol{E}$ is net positive, indicating electromagnetic energy transfer to particle energy. Near the EDR, the current sheet thins to approximately four to five electron skin depths (d_e). Within the thin current sheet, a narrow (two to three d_e) electron jet emerges. The Hall $\boldsymbol{E}$ presents a clear signature and the Hall-generated $\boldsymbol{B}$ is identifiable, albeit with fluctuations. Of particular interest, we show that the electron jet transports sufficient off-diagonal momentum to support the concept that off-diagonal electron pressure or electron inertial stress sustains the reconnection $\boldsymbol{E}$ in the turbulent EDR (Hesse et al. 2014, 2018; Burch et al. 2016; Nakamura et al. 2018; Torbert et al. 2018).

2. Observations

Figure 1 displays 1 hr of observations (Ergun et al. 2016a; Blake et al. 2016; Lindqvist et al. 2016; Pollock et al. 2016; Russell et al. 2016; Torbert et al. 2016) that include a 30-minute period of turbulence, demarcated with vertical dashed lines. The event is in Earth's magnetotail ~ 25 R_E (Earth radius) from Earth's center; the GSE (geocentric solar ecliptic) location is above the figure. Figure 1(a) displays $\boldsymbol{B}$ in GSE coordinates. The colors represent directions and the black trace is $|\boldsymbol{B}|$. Immediately below, Figure 1(b) displays $\boldsymbol{B}$ with 10 s detrending, $d\boldsymbol{B} = \boldsymbol{B} - \langle\boldsymbol{B}\rangle_{10s}$, which highlights $\boldsymbol{B}$ fluctuations. At the beginning of Figure 1(a), the MMS satellites are in the southern lobe as evidenced by negative B_x, the blue trace. From $\sim 12{:}13$ to $\sim 12{:}43$ UT, the MMS satellites are in a region of strong turbulence with $|\Delta\boldsymbol{B}|/|\boldsymbol{B}|$ near unity and intensely fluctuating $\boldsymbol{E}$ (Figure 1(c)).

Figure 1(d) plots $\boldsymbol{V}_{\mathrm{Ion}}$, the ion velocity. $\boldsymbol{V}_{\mathrm{Ion}}$ is difficult to interpret prior to $\sim 12{:}15$ UT because the plasma density (N_e, Figure 1(e)) is extraordinarily low in the lobe. The anti-Earthward $\boldsymbol{V}_{\mathrm{Ion}}$ (blue trace is negative) at $\sim 12{:}04$ UT suggests that a reconnection event began Earthward of the MMS satellites (see cartoon, Figure 2(a)). At $\sim 12{:}15$ UT, N_e increases allowing for validation that $\boldsymbol{V}_{\mathrm{Ion}}$ is anti-Earthward. The anti-Earthward flow (Figure 1(d), blue trace) reverses at $\sim 12{:}16$ UT indicating a magnetic reconnection event retreated anti-Earthward of the MMS satellites. The $\boldsymbol{V}_{\mathrm{Ion}}$ reversal and fluctuations (Figure 1(d)), strong fluctuations in $\boldsymbol{B}$ (Figures 1(a) and (b)) and intense variations in $\boldsymbol{E}$ (Figure 1(c)) are signatures of turbulent magnetic reconnection (Ergun et al. 2018, 2020a, 2020b).

Figures 1(f) and (g) display ion fluxes as a function of energy. Details are in the figure caption. Immediately below, Figures 1(h) and (i) show electron fluxes. The salient features of these observations are variations in energetic ion (Figure 1(f)) and electron fluxes (Figure 1(h)), which suggest local particle acceleration during the magnetic reconnection-driven turbulence (Ergun et al. 2020a, 2020b).

Figure 2(b) plots the power spectral density (PSD) of $\boldsymbol{B}$ and $\boldsymbol{E}$ as a function of frequency. Each of the $\boldsymbol{B}$ and $\boldsymbol{E}$ PSDs is separated into low-frequency spectra that include the entire 30-minute turbulent interval and high-frequency spectra that are compiled over a shorter interval when high-resolution "burst" data are available (Burch et al. 2016). The low-frequency PSD of $\boldsymbol{B}$ displays a spectral break slightly below f_{ci}, which is consistent with $kd_i \sim 1$ (k is the wavevector and d_i is the ion skin depth). The lower-frequency (inertial) region has a shallower index than the
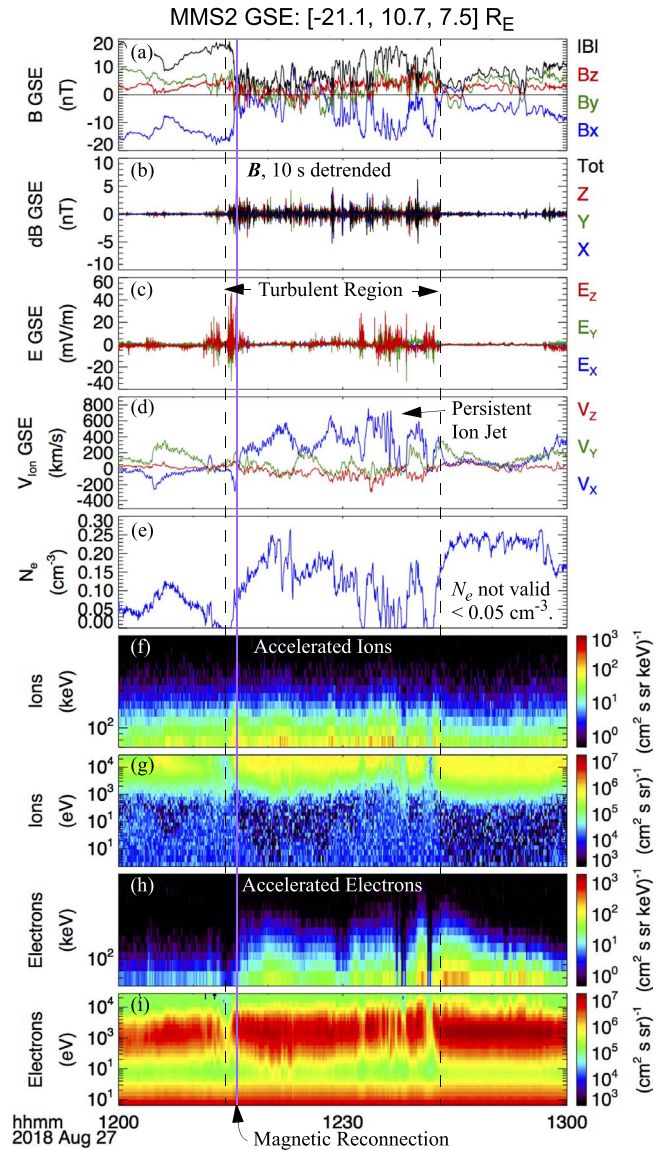
Figure 1. A turbulent magnetic reconnection region in Earth's magnetotail. (a) $\boldsymbol{B}$ at 64.5 ms resolution. (b) $\boldsymbol{B}$ detrended by 10 s. (c) $\boldsymbol{E}$ at 31.25 ms resolution. (d) $\boldsymbol{V}_{\mathrm{Ion}}$ at 4.5 s resolution. (e) N_e at 30 ms resolution. (f) Ion flux from 70 to 600 keV. (g) Differential ion energy flux from 3 eV to 25 keV. (h) Electron flux from 60 to 500 keV. (i) Differential electron energy flux from 6 eV to 25 keV.

near-Kolmogorov indexes previously reported (Stawarz et al. 2015; Ergun et al. 2015; Ergun et al. 2020a, 2020b), which may be due to the large range of $|\boldsymbol{B}|$ and N_e. The PSD of $\boldsymbol{E}$ shows a buildup of electrostatic or Hall $\boldsymbol{E}$ (-0.8 index) as often seen in magnetotail turbulence. The probability distribution function (not shown) of increments of $\boldsymbol{B}$ has larger kurtosis for short intervals than for long intervals, indicating intermittent turbulence (Stawarz et al. 2015). In short, the observations are consistent with intermittent turbulence that is not fully developed. $\boldsymbol{J} \cdot \boldsymbol{E}$ (Figure 2(c)) is net positive, supporting particle energization.
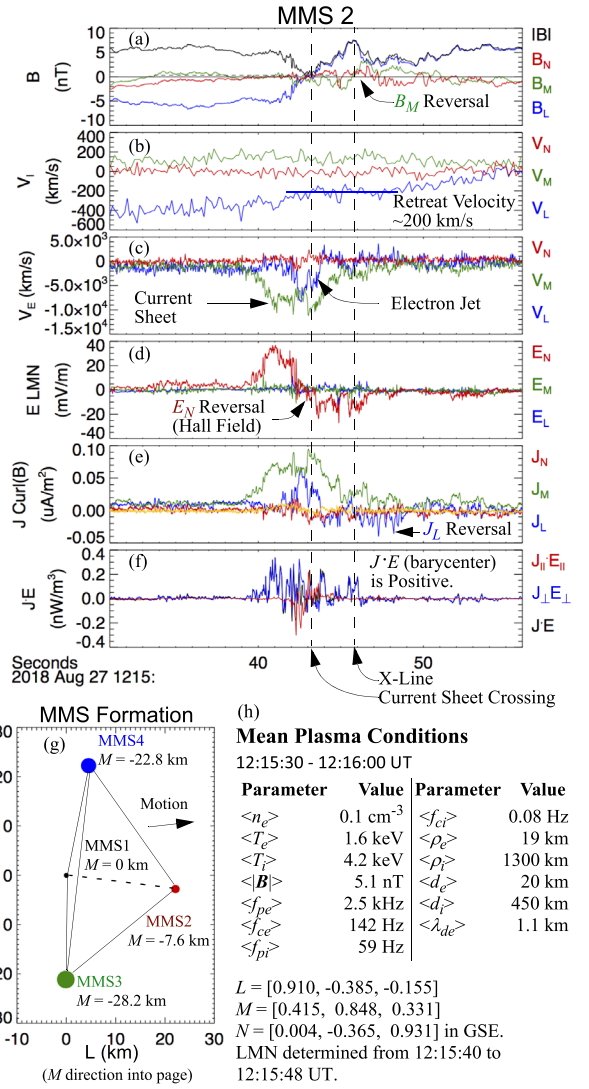
In a cursory analysis, two well-studied current sheet instabilities can be identified. A plasmoid-like instability (e.g., Huang & Bhattacharjee 2016) appears to be active after $\sim 12{:}30$ UT (see modulations in the ion jet; Figure 1(d)) and a type of drift wave is present (Wang et al. 2022). Nonetheless, the reconnection rate is roughly 0.1–0.2 using an average
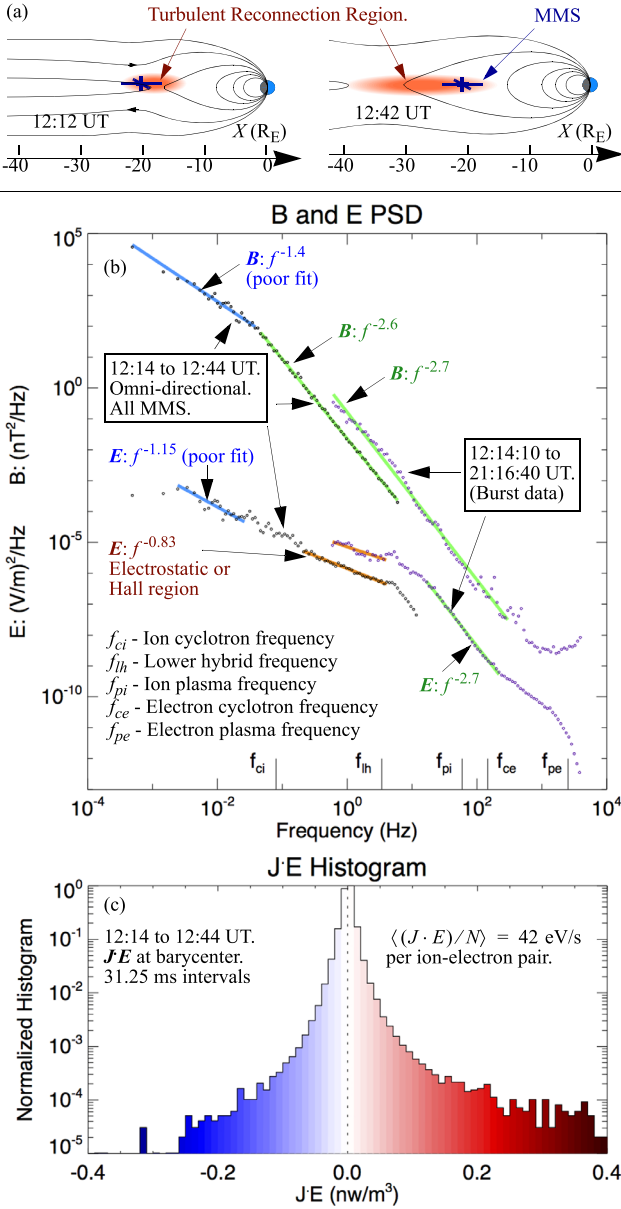
Figure 2. (a) A cartoon of a retreating X-line and expanding region of turbulence. (b) **B** and **E** power spectral density. The low-frequency spectra are from the entire 30-minute turbulent period. The high-frequency spectra are from a ~2 1/2 minute period when burst data are available. (c) A histogram of $J \cdot E$ showing net particle energization.

Figure 3. Near-EDR observations. The vertical dashed lines indicate (left) the current sheet and (right) the X-line retreating past MMS. Vectors are in *LMN* coordinates. (a) **B** at 128 samples s^{-1}. (b) V_{Ion} at 150 ms resolution. (c) V_{Elc} at 30 ms resolution. V_{Elc} is derived from integration of the electron distribution. (d) **E** at 8192 samples s^{-1}. (e) **J** derived from $\nabla \times B / \mu_o$ at 128 samples s^{-1}. The orange trace is $\nabla \cdot B / \mu_o$, which is a measure of the accuracy of **J**. (f) $J \cdot E$ at the MMS barycenter at 128 samples s^{-1}. (g) MMS formation in *LMN*. (h) Plasma conditions and *LMN* values.

Alfvén velocity (1000 km s^{-1}) and an estimated reconnection E of ~1.5 mV m^{-1} (see later).

Figure 3 displays a rare case in which the EDR of turbulent magnetic reconnection can be identified (see the vertical magenta line; Figure 1). This event is of great interest because magnetic reconnection in turbulence has been, for the most part, inferred (e.g., by ion jet reversal). Figures 3(a)–(f), display **B**, V_{Ion}, V_{Elc} (electron velocity), **E**, **J** derived from $\nabla \times B / \mu_o$, and $J \cdot E$ over a 25 s period inside of the turbulent region (Figure 1(a)). These data are plotted in an orthonormal *LMN* coordinate system (Denton et al. 2018) in which *L* represents the primary direction of reversing **B**, *M* is along the X-line, and *N* is the current sheet normal. Because of the turbulence, *LMN* directions are not derived by a conventional method (Denton et al. 2018). *L* is set by the maximum variance of **B**, but the **B** variance analysis does not separate *M* and *N* well. *N* is set by the maximum variance of **E** (Figure 3(d)). Fortunately, *L* and *N* are nearly perpendicular, requiring only minor adjustments. The *M* direction follows. *L*, *M*, and *N* are recorded in Figure 3(h).

Figure 3 reveals nearly antiparallel magnetic reconnection. $B_M = -0.5$ nT (Figure 3(a)) when $B_L = 0$ (Figure 3, left vertical dashed line), allowing for a small guide field (Tang et al. 2022). However, fluctuations in B_M are up to 2 nT, making the guide field unresolved. A Hall electron current sheet is seen at ~12:15:43 UT (left vertical dashed line). The *M* component of V_{Elc} (Figure 3(c), green trace) is centered when $B_L \sim 0$ (Figure 3(a), blue trace) and E_N is reversing (Figure 3(d), red trace). The current sheet (Figures 3(c) and (e), green traces) has a slight bifurcation (a depression in the middle, 12:15:43 UT), which suggests that MMS2 is just outside of the EDR. A narrow electron jet in the –*L* direction is embedded in the
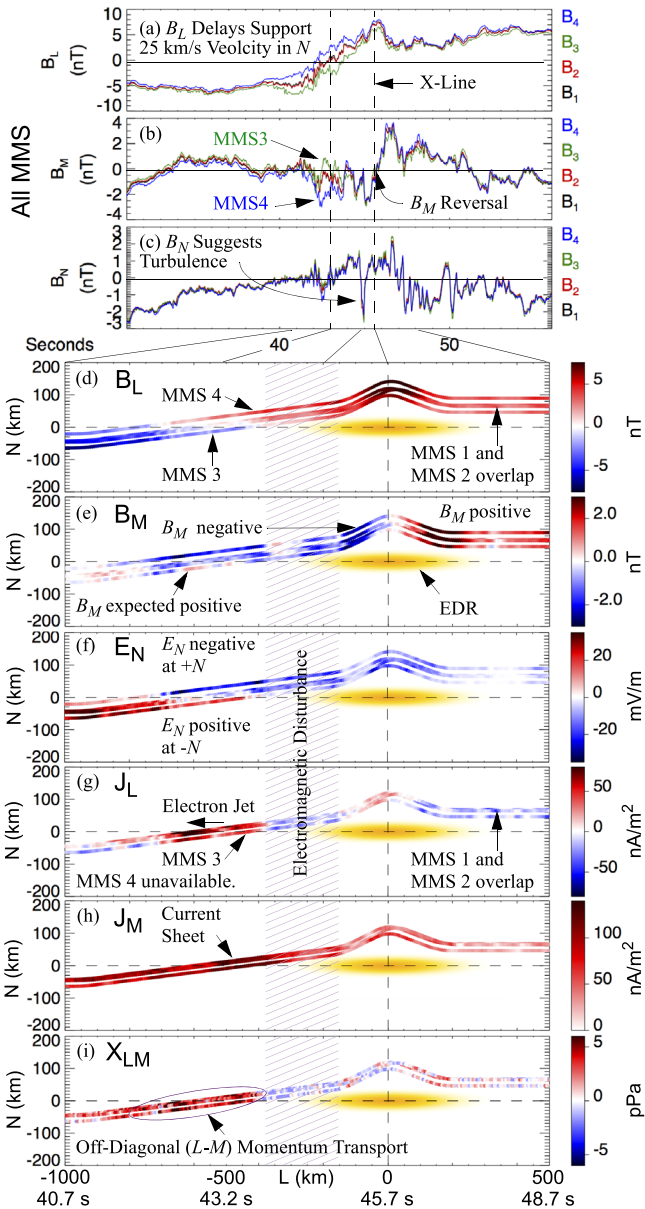
Figure 4. (a), (b), and (c) B_L, B_M, and B_N from the four MMS satellites. $\boldsymbol{B}$ shows higher fluctuations than observed in laminar magnetic reconnection. (d)–(i) The smoothed path of the MMS satellites with respect to the X-line constructed using the retreat velocity (200 km s^{-1} in L) and time delays in B_L for N velocity over four segments. The values of B_L, B_M, E_N, J_L, J_M, and X_{LM} are represented by color. The shaded region marks a possible electromagnetic deflection of J_L. J_L, J_M, and X_{LM} are derived by integration of electron distributions from the MMS database; they are not the moments in the database.

electron current sheet (Figure 3(c), blue trace), insinuating that MMS2 is close (<1 d_i) to the EDR on the –L side. $\boldsymbol{J}$ derived from $\nabla \times \boldsymbol{B}/\mu_o$ (Figure 3(e), green trace) yields a net positive $\boldsymbol{J} \cdot \boldsymbol{E}$ (Figure 3(f)), also supporting that the MMS2 is near the EDR. $\boldsymbol{V}_{Ion}$ is ~200 km s^{-1} in the –L direction (Figure 3(b), blue trace) near the X-line, which we interpret as the retreat speed of the X-line (see Figure 1(i)). Figure 3(f) plots the MMS formation, and Figure 3(g) summarizes the plasma environment.

Figures 4(a)–(c) display, in order, B_L, B_M, and B_N from all of the MMS satellites over the same period as in Figure 3. The

colors designate the satellite. B_L signals (Figure 4(a)) show that MMS4 (blue trace) crosses the current sheet prior to MMS1 and MMS2, followed by MMS3 (green trace). During the current sheet crossing, B_L time delays support an average speed of ~25 km s^{-1} in the N direction. The MMS satellites can be thought to be moving 200 km s^{-1} in the +L direction ($-\boldsymbol{V}_{Ion}$ retreat speed) and 25 km s^{-1} in the +N direction with respect to the X-line as they cross the current sheet.

Turbulence is apparent in all components of $\boldsymbol{B}$. B_M, the Hall magnetic field, is expected to be positive prior to crossing the current sheet and then turn negative. While B_M is positive a few seconds before crossing the current sheet (Figure 4(b), 34 s to 38 s), it fluctuates between positive and negative before crossing the current sheet at ~43 s. As discussed earlier, a small guide field may be present, but fluctuations dominate. As expected, B_M remains mostly negative after crossing the current sheet and then becomes positive again at ~45.7 s, indicating that MMS moved to the +L side of the X-line. B_N (Figure 4(c)) also shows fluctuations. A roughly −4 nT excursion in B_N at ~45 s concurrently with ~5 mV m^{-1} excursions in E_L and E_M indicate an electromagnetic disturbance. A time-delay analysis indicates a high speed (>500 km s^{-1}).

Figures 4(d)–(i) display plausible paths of the MMS satellites with respect to the X-line in L (horizontal axis) and N (vertical axis). The magnified view covers 8 s. The paths assume a 200 km s^{-1} velocity in L. The N velocities and positions are derived from time delays in B_L in four segments and are consistent with $\nabla \times \boldsymbol{B} = \mu_o \boldsymbol{J}$, which is dominated by B_L and J_M. Figures 4(d)–(f) each have four traces, one per MMS satellite. MMS4 is on the +N side and MMS3 is on the −N side (see Figure 3(g)). MMS1 and MMS2 traces overlay. The colors of the traces represent the measured values of B_L, B_M, and E_N, respectively. B_L (Figure 4(d)) and E_N (Figure 4(f)) are fairly well behaved at the current sheet crossing ($N = 0$), which is somewhat expected because L and N are, respectively, the maximum variance of $\boldsymbol{B}$ and the maximum variance of $\boldsymbol{E}$. However, all of the E_N and B_L reversals are at $N = 0$ (defined for MMS1), even at different locations in L and at different times. This well-behaved pattern supports that LMN is well determined and that the paths are reasonable.

Figure 4(g) displays J_L derived from the ion and electron distributions as $eN(\boldsymbol{V}_{Ion} - \boldsymbol{V}_{Elc})$, where e is charge. MMS4 electron distributions are not available, so only three traces are displayed. J_L, dominated by the electron jet, is centered in the current sheet (Figure 4(g), ~43 s, $L = -450$ km). All three traces of J_L are abruptly deflected or disrupted near-simultaneously, indicating a temporal change, which is the shaded region in Figures 3(d)–(i) (~44 to ~45 s). Afterward, J_L behaves as expected. It reverses polarity at $L = 0$, consistent with passing the X-line. J_M (Figure 4(h)) is positive throughout, which indicates that the Hall electron current sheet is embedded in a larger-scale current sheet. The electron current sheet is between 3 and 5 d_e thick in N and the electron jet, J_L, appears to be between 2 and 3 d_e thick in N as expected at the outer edge of the EDR.

Figure 4(i) displays the L–M element of the electron stress tensor $\overline{\overline{X}} = nm_e\overline{\boldsymbol{V}}_{Elc}\overline{\boldsymbol{V}}_{Elc} + \overline{\overline{P_e}}$, where m_e is electron mass and $\overline{\overline{P_e}}$ is electron pressure. X_{LM} peaks at ~8 pPa and averages 3.5 pPa during the current sheet crossing (42.1 s to 43.7 s). Importantly, X_{LM} establishes that momentum in the M direction is being transported laterally in the L direction from the EDR.
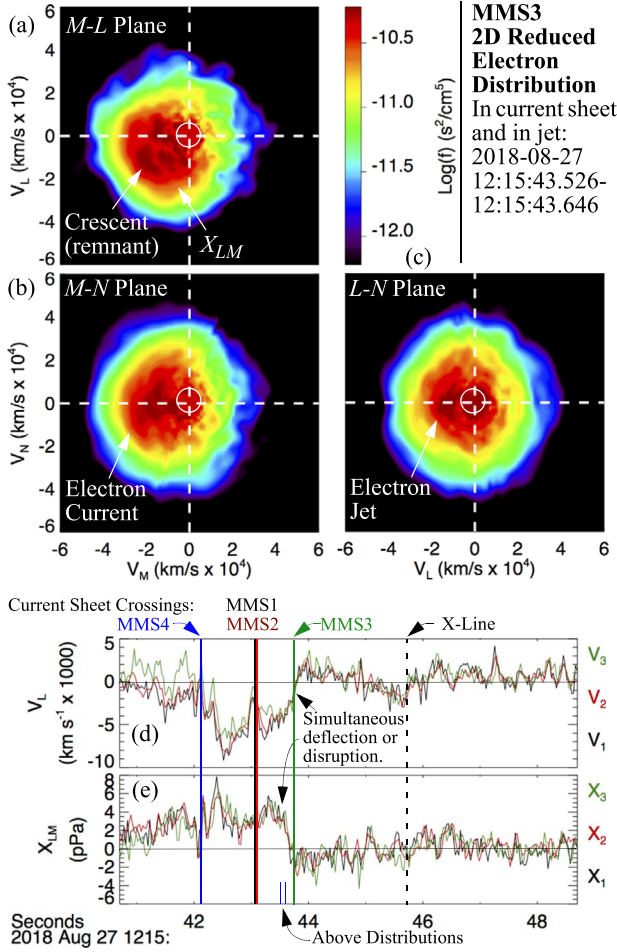
Figure 5. The electron distribution in the current sheet and in the jet as it emerges from the EDR (see Figure 4). (a) Off-diagonal stress is evident in the *M–L* plane. Crescent-shaped structures are visible. (b) The *M–N* plane shows the current sheet and (c) the *L–N* plane shows the electron jet. There is a large uncertainty inside the white circle due to spacecraft photoelectrons. (d) and (e) Electron V_L and X_{LM} from MMS1, MMS2, and MMS3.

3. Off-diagonal (*L–M*) Stress and EDR Behavior in Turbulence

X_{LM} (Figure 4(i)) is telling of electron behavior in the EDR, in particular, how the reconnection electric field (E_M) may be supported. X_{LM} is between 2 and 3 d_e wide in N, which is roughly the expected thickness of the EDR. Figures 5(a)–(c) display three planes of an electron distribution from MMS3 in the jet and in the current sheet close to the EDR. Four, 30 ms electron distributions are averaged to reduce noise and variations driven by turbulence. Off-diagonal stress is visible in the *M–L* plane (Figure 5(a)). Crescent-shaped structures, a signature of magnetic reconnection (Hesse et al. 2014, 2018; Burch et al. 2016; Nakamura et al. 2018; Torbert et al. 2018), are weak but visible in all three planes in Figure 5. Interestingly, ~75% of the off-diagonal stress is carried by $nm_e \overline{V}_{Elc}\overline{V}_{Elc}$ (inertial stress) whereas ~25% is carried by off-diagonal $\overline{\overline{P}}_e$. Because this distribution is outside of the EDR at $L = -400$ km, ~20 d_e from the X-line, this finding is not in conflict with previous studies (Hesse et al. 2014, 2018; Burch et al. 2016; Nakamura et al. 2018; Torbert et al. 2018) that conclude that an off-diagonal gradient in $\overline{\overline{P}}_e$ dominates inside of the EDR. Rather, it supports these studies.

Figures 5(d) and (e) display the time series of electron V_L and X_{LM} from MMS1, MMS2, and MM3. Of particular interest, V_L and X_{LM} vary near-simultaneously in time even though the MMS spacecraft are widely separated with respect to the current sheet (see the vertical lines in Figures 5(d) and (e); also see Figure 3(g)). This behavior suggests that turbulent fluctuations are deflecting or modulating the electron jet in time. For example, variations in B_M can deflect the electron jet in the N direction while variations in B_N can deflect it in the M direction. Figures 5(d) and (e) indicate that the electron jet variations outside of the EDR are dominated by turbulent fluctuations.

An estimation of $\langle \delta \boldsymbol{B} \times \delta \boldsymbol{J} \rangle / en_e$ shows that it is insufficient to support E_M in the EDR (Tang et al. 2022). Our estimation comes to the same conclusion. Here, we examine X_{LM} to determine if electron stress can support E_M in this turbulent EDR (Hesse et al. 2018):

$$E_M \approx -\frac{1}{en}\left(\frac{\partial X_{LM}}{\partial L} + \frac{\partial X_{NM}}{\partial N}\right).$$

Assuming that the EDR extends 10 d_e in L from the X-line, that X_{LM} represents the lateral transport of M momentum out of the EDR, and that $X_{LM} = 0$ at $L = 0$ (X-line), the X_{LM} contribution to E_M is ~1.4 mV m^{-1} when setting $\Delta X_{LM} = 3.5$ pPa and $\Delta L = 10d_e$. In another approach, Hesse et al. (1999) estimate

$$E_M \approx -\frac{1}{e}\frac{\partial V_L}{\partial L}\sqrt{\frac{m_e T_e}{2}},$$

E_M is ~1.7 mV m^{-1} using $\Delta V_L = 5 \times 10^6$ m s^{-1}, and $T_e = 1.6$ keV (Figure 3(h)). These two estimated values of E_M are consistent with previously measured E_M values in Earth's magnetotail (Genestreti et al. 2018; Torbert et al. 2018). Ideally, one compares these values with measured E_M. However, turbulence, uncertainty in the *LMN* directions (Genestreti et al. 2018) and uncertainty in E (Ergun et al. 2016a; Lindqvist et al. 2016; Torbert et al. 2016) result in a significant ambiguity.

Averaging E_M and $-(V_{Elc} \times \boldsymbol{B})_M$ from MMS1, MMS2, and MMS3 in the well-behaved period in the current sheet (12:15:42.1 to 12:1543.7 UT) yields 1.3 mV m^{-1} with a range from 0.4 to 2.2 mV m^{-1}. MMS4 has no V_{Elc} determination and the least-accurate E measurement, so it is not used. Using different time periods results in a larger range (e. g. Tang et al. 2022) but suggests E_M is on the order of 1–2 mV m^{-1}. Despite the difficulty in establishing E_M, one can come to a meaningful conclusion that the measured X_{LM} in the electron jet suggests that electron stress can support E_M in the turbulent EDR.

4. Conclusions

Overall, MMS observations reveal that magnetic reconnection advances in a turbulent environment with many of the same properties and processes of laminar, 2D magnetic reconnection. Figure 1(d) shows a persistent ion jet, indicating that a dominant EDR perseveres despite the turbulence. Near the EDR, the magnetic field reversal (B_L; Figures 3(a), 4(a), and (d)), the Hall electric field (E_N; Figures 3(d) and 4(f)), and the current sheet (J_M; Figures 3(e) and 4(h)) behave as understood from laminar magnetic reconnection, albeit with fluctuations. The Hall magnetic field (B_M; Figures 3(a), 4(b), and (e)), B_N (Figures 3(a) and 4(c)), the electron jet (J_L; Figures 3(c) and 4(g)) and, most interestingly, the electron stress (X_{LM};

Figure 4(i)) also have similar properties to those expected in laminar magnetic reconnection. B_M and B_N, however, are more active and an electromagnetic disturbance appears to have briefly deflected or disrupted J_L and X_{LM}. These observations suggest the electron-scale physics in a turbulent EDR does not necessarily differ from that in a laminar EDR.

That magnetic reconnection can be sustained in turbulence has noteworthy implications on particle acceleration. Magnetic reconnection enables magnetic field energy annihilation over a much larger volume than that of the ion diffusion region (Ergun et al. 2020a, 2020b), which results in local particle energization. Turbulent E and B can lead to substantial particle acceleration. These findings imply that particle acceleration can be sustained as well.

ORCID iDs

R. E. Ergun https://orcid.org/0000-0002-3096-8579
J. L. Burch https://orcid.org/0000-0003-0452-8403
R. B. Torbert https://orcid.org/0000-0001-7188-8690
A. Chasipis https://orcid.org/0000-0001-8478-5797
D. L. Newman https://orcid.org/0000-0003-0810-1204
J. E. Stawarz https://orcid.org/0000-0002-5702-5802
D. L. Turner https://orcid.org/0000-0002-2425-7818
D. Gershman https://orcid.org/0000-0003-1304-4769

References

Blake, J. B., Mauk, B. H., Baker, D. N., et al. 2016, SSRv, 199, 309
Burch, J. L., Moore, T. E., Torbert, R. B., & Giles, B. L. 2015, SSRv, 199, 5
Burch, J. L., Torbert, R. B., Phan, T. D., et al. 2016, Sci, 352, aaf2939
Cozzani, G., Khotyaintsev, Yu. V., Graham, D. B., et al. 2021, PhRvL, 127, 215101
Daughton, W. 2003, PhPl, 10, 3103
Denton, R. E., Sonnerup, B. U. Ö., Russell, C. T., et al. 2018, JGRA, 123, 2274
Drake, J. F., Shay, M. A., & Swisdak, M. 2008, PhPl, 15, 042306
Eastwood, J. P., Phan, T. D., Bale, S. D., et al. 2009, PhRvL, 102, 035001
Eastwood, J. P., Phan, T. D., Øieroset, M., & Shay, M. A. 2010, JGRA, 115, A08215
Ergun, R. E., Ahmadi, N., Kromyda, L., et al. 2020a, ApJ, 898, 154
Ergun, R. E., Ahmadi, N., Kromyda, L., et al. 2020b, ApJ, 898, 153
Ergun, R. E., Goodrich, K., Wilder, F., et al. 2016b, PhRvL, 116, 235102
Ergun, R. E., Goodrich, K. A., Stawarz, J. E., Andersson, L., & Angelopoulos, V. 2015, JGRA, 120, 1832
Ergun, R. E., Goodrich, K. A., Wilder, F. D., et al. 2018, GeoRL, 45, 3338
Ergun, R. E., Tucker, S., Westfall, J., et al. 2016a, SSRv, 199, 167
Genestreti, K. J., Nakamura, T. K. M., Nakamura, R., et al. 2018, JGRA, 123, 9130
Gosling, J. T. 2007, ApJL, 671, L73
Gosling, J. T., Skoug, R. M., McComas, D. J., et al. 2005, JGR, 110, A01107
Hesse, M., Aunai, N., Sibeck, D., & Birn, J. 2014, GeoRL, 41, 8673
Hesse, M., Norgren, C., Tenfjord, P., et al. 2018, PhPl, 25, 032901
Hesse, M., Schindler, K., Birn, J., & Kuznetsova, M. 1999, PhPl, 6, 1781
Huang, Y.-M., & Bhattacharjee, A. 2016, ApJ, 818, 20
Ji, H., Terry, S., Yamada, M., et al. 2004, PhRvL, 92, 115001
Lapenta, G., Krauss-Varban, D., Karimabadi, H., et al. 2006, GeoRL, 33, L10102
Lindqvist, P. A., Olsson, G., Torbert, R. B., et al. 2016, SSRv, 199, 137
Nakamura, R., Genestreti, K. J., Nakamura, T. K. M., et al. 2019, JGRA, 124, 1173
Nakamura, T. K. M., Genestreti, K. J., Liu, Y.-H., et al. 2018, JGRA, 123, 9150
Øieroset, M., Phan, T., Fujimoto, M., Lin, R., & Lepping, R. 2001, Natur, 412, 414
Phan, T. D., Eastwood, J. P., Shay, M. A., et al. 2018, Natur, 557, 202
Pollock, C., Moore, T., Jacques, A., et al. 2016, SSRv, 199, 331
Price, L., Swisdak, M., Drake, J. F., et al. 2016, GeoRL, 43, 6020
Price, L., Swisdak, M., Drake, J. F., et al. 2017, JGRA, 122, 11086
Pritchett, P. L., Mozer, F. S., & Wilber, M. 2012, JGRA, 117, A06212
Retinó, A., Sundkvist, D., Vaivads, A., et al. 2007, NatPh, 3, 236
Roytershteyn, V., Dorfman, S., W. Daughton, W., et al. 2013, PhPl, 20, 061212
Russell, C. T., Anderson, B. J., Baumjohann, W., et al. 2016, SSRv, 199, 189
Stawarz, J. E., Eastwood, J. P., Phan, T. D., et al. 2019, ApJL, 877, L37
Stawarz, J. E., Ergun, R. E., & Goodrich, K. A. 2015, JGRA, 120, 1845
Tang, B.-B., Li, W. Y., Khotyaintsev, Y., et al. 2022, GeoRL, 49, e97573
Torbert, R. B., Burch, J. L., Phan, T. D., et al. 2018, Sci, 362, 1391
Torbert, R. B., Russell, C. T., Magnes, W., et al. 2016, SSRv, 199, 105
Wang, S., Chen, L.-J., Bessho, N., et al. 2022, JGRA, 127, e30109